

# Unsupervised Neural-Implicit Laser Absorption Tomography for Quantitative Imaging of Unsteady Flames

Joseph P. Molnar<sup>1,\*</sup>, Jiangnan Xia<sup>2,3,\*</sup>, Rui Zhang<sup>2</sup>, Samuel J. Grauer<sup>1</sup>, and Chang Liu<sup>2,†</sup>

<sup>1</sup>Department of Mechanical Engineering, Pennsylvania State University

<sup>2</sup>School of Engineering, University of Edinburgh

<sup>3</sup>School of Mechanical Engineering, Shanghai Jiao Tong University

## Abstract

This paper presents a novel neural-implicit approach to laser absorption tomography (LAT) with experimental verification. A coordinate neural network is used to represent thermochemical state variables as continuous functions of space and time. Unlike most existing neural methods for LAT, which rely on prior simulations and supervised training, our approach is based solely on LAT measurements, utilizing a differentiable observation operator with line parameters provided in standard spectroscopy database formats. Although reconstructing scalar fields from multi-beam absorbance data is an inherently ill-posed, nonlinear inverse problem, our continuous space–time parameterization supports physics-inspired regularization strategies and enables physics-informed data assimilation. Synthetic and experimental tests are conducted to validate the method, demonstrating robust performance and reproducibility. We show that our neural-implicit approach to LAT can capture the dominant spatial modes of an unsteady flame from very sparse measurement data, indicating its potential to reveal combustion instabilities in measurement domains with minimal optical access.

**Keywords:** laser absorption tomography, quantitative imaging, inverse problems, neural-implicit reconstruction technique, combustion diagnostics

## 1 Introduction

Turbulent mixing and combustion are fundamental processes in power and propulsion systems [1]. These applications often involve complex, unsteady thermochemical fields that require advanced experimental techniques for accurate characterization. Spatio-temporally resolved data are essential for identifying turbulent structures. Optical diagnostics provide quantitative, non-intrusive one-, two-, and three-dimensional (1D/2D/3D) measurements at high repetition rates, making them indispensable for such studies. However, many spatially resolved sensors, including those based on laser-induced fluorescence [2, 3], filtered Rayleigh scattering [4, 5], particle image [6, 7] and tracking [8] velocimetry, or multi-angle light scattering [9], require extensive optical access to the probe volume. This limitation confines their use to controlled laboratory environments. Additionally, these techniques often demand complex optics and precise calibration, making them vulnerable in harsh environments characterized by vibrations, high heating loads, or window fouling. Pilot- and full-scale power and propulsion applications thus necessitate a robust, high-speed imaging technique capable of operating under adverse conditions with minimal optical access. This need motivates the development of a neural-implicit algorithm for laser absorption tomography (LAT) [10, 11], termed *NILAT*, a robust approach for reconstructing challenging flows from sparse LAT data.

Laser absorption tomography employs multi-beam absorption spectroscopy to reconstruct 2D fields of mole fraction, temperature, and, in certain setups, pressure [12] or velocity [13, 14]. LAT systems are flexible and accessible, often utilizing commercial telecom laser equipment and requiring only a few pencil-sized entry and exit points for the laser beams. This minimal optical access has enabled the deployment of LAT

\* Authors made an equal contribution.

† Corresponding author: [c.liu@ed.ac.uk](mailto:c.liu@ed.ac.uk)

across a wide range of power and propulsion systems, including automotive [15] and marine-engine pistons [16] for analyzing fuel-air mixing, industrial swirl combustors [17, 18] for assessing combustion efficiency and lean blowout limits, and gas turbine exhaust plumes [19] for monitoring carbon emissions. To achieve rapid imaging, LAT systems typically use a fixed array of beams. In small-scale setups, this may involve a few dozen beams, while larger systems have arrays of up to 150 beams [19–22].

Accurately inferring turbulent flow fields from LAT data has been a long-standing challenge [23]. Typically, the region of interest (RoI) is represented using a pixel or triangle-element basis, with the measurement equations discretized accordingly. This approach results in a linear inverse problem for each wavenumber in spectrally resolved LAT or for each transition in spectrally integrated LAT. A set of linear reconstructions can then be locally post-processed to calculate thermochemical and velocity fields, as discussed in [Appendix A.1](#). When the basis resolution is sufficiently high to capture the complexity of turbulent flows, the system of equations becomes underdetermined, as the number of basis functions,  $n$ , far exceeds the number of laser beams,  $m \ll n$ . This discrepancy necessitates regularization to produce unique, stable, and physically plausible reconstructions [23].

Iterative solvers, such as the algebraic reconstruction technique (ART) and its variants, have been widely used for decades [24, 25]. These solvers exhibit semi-convergence, where the first few iterations capture robust low-frequency components of the solution, while later iterations are increasingly affected by noise [26]. Early stopping can yield reasonable but low-resolution estimates, effectively acting as a form of *implicit* regularization. Optimizing the number of iterations is challenging, however, and ART reconstructions suffer from poor spatial fidelity compared to other algorithms. *Explicit* regularization techniques are generally preferred due to their accuracy, predictable impact on solutions, and support for uncertainty quantification (UQ) [27–29]. In LAT, explicit methods typically impose spatial smoothness, either globally using Tikhonov regularization or locally using total variation (TV) regularization for edge preservation. Statistical methods, particularly Bayesian inversion, are also widely employed to incorporate correlation length scales and to enable UQ [23, 27]. Among explicit methods, Tikhonov regularization is particularly popular in the LAT community due to its simplicity, acceptable accuracy, and computational efficiency [30–35]. Comprehensive reviews of regularization techniques for LAT are provided by Cai [10] and Liu [11].

Nonlinear methods for LAT directly parameterize reconstructions using temperature and mole fraction fields rather than absorbance fields, allowing regularization to be applied directly to these state variables [10, 29]. However, nonlinear LAT is inherently non-convex, typically requiring metaheuristic global optimization techniques. These approaches significantly increase computational costs and, in some cases, degrade solution quality [12]. Most advancements in nonlinear LAT algorithms have focused on optimizing the inversion process rather than addressing the spatial characteristics of the solution itself [32, 36–39]. Early nonlinear LAT algorithms employed spatial regularization strategies similar to those used in linear methods, such as Tikhonov or TV regularization, as discussed in [Appendix A.2](#).

A new generation of nonlinear LAT algorithms leverages modern machine learning methods, generally categorized as supervised or unsupervised approaches. Supervised methods train a neural network using labeled input–output data pairs to directly map projection datasets to field variables, such as mole fraction and temperature [40–46]. Network architectures range from advanced designs such as vision transformers [46] and long short-term memory networks [45] to simpler configurations, including multilayer perceptrons [40, 41], convolutional neural networks [42, 47], and extreme learning machines [43]. These methods are typically trained on synthetic data, often generated using Gaussian phantoms or computational fluid dynamics (CFD) simulations. However, supervised methods face significant limitations, including the challenge of constructing representative training sets for complex, real-world combustion scenarios and the difficulty of generalizing to unseen flow and combustion features.

The second machine learning approach to nonlinear LAT employs an explicit measurement operator to achieve a single reconstruction. Instead of learning a direct mapping from LAT projections to field variables, these methods use a “coordinate” neural network to represent the gas as a function of spatial and temporal inputs, known as a neural-implicit representation. The network is trained by minimizing discrepancies between actual projection data and synthetic projections of the neural-implicit field variables, computed through a high-fidelity, differentiable, and potentially nonlinear measurement operator. This approach, called the neural-implicit reconstruction technique (NIRT), has been successfully applied across various tomographic modalities, including X-ray radiography [48–51], emission imaging [52, 53], and schlieren-based techniques [54, 55]. NIRT is versatile, accommodating any LAT measurements regardless of the

sensor arrangement, and does not rely on prior information or training data.

Recently, Li et al. [56] proposed a NIRT algorithm for nonlinear LAT, representing the flow field with a coordinate neural network and using hyperspectral CO<sub>2</sub> absorbance data to recover *axisymmetric* temperature and mole fraction fields in steady flames. This approach is effective at reconstructing smooth, steady fields, benefiting from a network architecture that is inherently biased toward low-frequency solutions: a form of implicit regularization that mitigates the problem of rank-deficiency in LAT. However, the method struggles with low signal-to-noise ratios (SNRs) and sparse data. A key challenge moving forward is to develop LAT methods capable of addressing more complex scenarios, such as reconstructing 2D distributions in unsteady, turbulent flames with transient and asymmetric structures. Current linear and nonlinear LAT algorithms, including Li et al.’s NIRT technique, lack the robustness required to reconstruct high spatial frequency content from sparse measurements.

Our NILAT framework builds on the method of Li et al., incorporating a differentiable, nonlinear absorption measurement operator grounded in fundamental spectroscopic relationships and line parameters to compute synthetic projections from the network outputs. Unlike Li’s algorithm, which performs radial inversions at discrete time instances, NILAT represents time-resolved field variables within the measurement plane, enabling a single-step “2D + *t*” reconstruction over an extended measurement interval. By solving the reconstruction problem for the entire time series simultaneously, NILAT leverages the regularities and sparsity of the spatio-temporal dynamics of the flow/combustion system to improve accuracy. It also incorporates a Fourier encoding to capture broadband spectral content and employs explicit regularization to ensure physically plausible results. Additionally, NILAT readily facilitates data assimilation based on the governing equations of the target process.

The remainder of this paper details the working principles of LAT, our reconstruction framework, and the selection of regularization parameters for ill-posed inverse problems. Section 4 describes the flames considered in this study. Section 5.2 presents a parametric characterization of NILAT, and Sec. 5.3 examines the results of three experimental cases, highlighting flame dynamics in the burners and concluding with insights into the proposed methodology.

## 2 Neural-Implicit Laser Absorption Tomography

Laser absorption tomography extends laser absorption spectroscopy by utilizing multiple laser beams to capture spatially resolved information about a gas-phase species. By measuring light attenuation at various wavenumbers along these paths, LAT enables the inference of key properties such as temperature, chemical composition, velocity, and pressure. This section reviews the measurement model for absorption spectroscopy and introduces our neural reconstruction strategy for LAT. The NILAT framework is followed by an overview of regularization techniques.

### 2.1 Absorption Spectroscopy Preliminaries

The fundamental quantity in absorption spectroscopy is the spectral absorbance,

$$\alpha_\nu \equiv \log\left(\frac{I_{0,\nu}}{I_\nu}\right) = \int_0^L \kappa_\nu[\mathbf{r}(s)] ds, \quad (1)$$

where  $\nu$  is the detection wavenumber and  $I_{0,\nu}$  and  $I_\nu$  are the non-absorbing reference (flame-off) and attenuated (flame-on) intensities incident on the photodetector. The right-hand side of this expression follows from the Beer–Lambert law, where  $\kappa_\nu$  is the local absorption coefficient, and the indicator function  $\mathbf{r} : \mathbb{R} \rightarrow \mathbb{R}^2$  or  $\mathbb{R}^3$  represents the beam path. This function,  $\mathbf{r}$ , maps a progress variable,  $s$ , to a position along the beam of length  $L$ , defined such that  $|\mathbf{dr}/ds| = 1$ . Integrating over an absorption transition yields

$$A_k = \int_0^\infty \alpha_\nu d\nu = \int_0^L K_k[\mathbf{r}(s)] ds, \quad (2a)$$

where

$$K_k = \int_0^\infty \kappa_\nu d\nu = S_k(T) \frac{\chi P}{k_B T}. \quad (2b)$$

Here,  $A_k$  and  $K_k$  denote the path-integrated absorbance and local absorption coefficient for the  $k$ th transition of the target species. The right-hand side of Eq. (2b) connects the absorption coefficient to the thermody-

namic state of the gas, where  $S_k$  is the line strength for the  $k$ th transition,  $T$  is the gas temperature,  $\chi$  is the mole fraction of the target species,  $p$  is the pressure, and  $k_B$  is the Boltzmann constant.

The line intensity for transitions of common gases in local thermodynamic equilibrium can be computed using line parameters from spectroscopy databases, such as HITRAN [57, 58] or HITEMP [59], as follows:

$$S_k = S_{\text{ref},k} \frac{Q(T_{\text{ref}})}{Q(T)} \frac{\exp(-c_2 E_k''/T)}{\exp(-c_2 E_k''/T_{\text{ref}})} \frac{1 - \exp(-c_2 \nu_k/T)}{1 - \exp(-c_2 \nu_k/T_{\text{ref}})}. \quad (3)$$

In this expression,  $T_{\text{ref}}$  is a reference gas temperature (commonly 296 K),  $S_{\text{ref},k}$  is the line intensity at  $T_{\text{ref}}$ ,  $Q$  is the total internal partition sum (TIPS) function,  $c_2$  is the second radiation constant,  $E_k''$  is the lower-state energy of the  $k$ th transition, and  $\nu_k$  is the line center of the  $k$ th transition. The line center shifts based on the local thermochemical state and bulk gas velocity, a factor that must be accounted for in LAT when performing velocimetry. However, as this shift has a negligible effect on  $S_k$ , we approximate  $\nu_k$  with the vacuum line center,  $\nu_{0,k}$ , in this paper.

## 2.2 Neural-Implicit Reconstruction Technique

Equations (1) to (3) enable calculation of the absorbance for a specific laser beam given: (i) knowledge of the gas state,  $(\chi, T, p)$ , along the beam, (ii) line parameters of the target molecule,  $\{S_{\text{ref},k}, E_k'', \nu_{0,k}\}$  for each measured transition,  $k \in \mathcal{K}$ , and (iii) the molecule’s TIPS function,  $Q$ . While line parameters and TIPS functions are readily available in databases such as HITRAN and HITEMP, the gas state is typically unknown and must be reconstructed from multi-beam absorbance data. This section introduces the neural-implicit reconstruction technique for LAT, referred to as NILAT.

We begin with a set of simultaneous absorbance measurements,  $\{A_{k,i}(t)\}$ , indexed by  $i$  for each laser beam in the set  $\mathcal{I}$  and recorded at discrete time instances  $t_j$  for  $j \in \mathcal{J}$ . The goal is to reconstruct continuous 2D distributions of the target mole fraction,  $\chi$ , and gas temperature,  $T$ , that match these measurements. To achieve this, we represent the gas using neural states,

$$\mathcal{N} : (\mathbf{x}, t) \mapsto (\chi, T), \quad (4)$$

where  $\mathcal{N}$  is a deep feed-forward neural network that maps a spatial coordinate,  $\mathbf{x}$ , and time,  $t$ , to the quantities of interest. Details of the network architecture are provided in [Appendix B](#), and the framework can be extended to include additional state variables as needed.

The network is trained to reproduce measured data while conforming to prior information about the spatio-temporal dynamics of  $(\chi, T)$ . These objectives are encapsulated in a data fidelity term,  $\mathcal{L}_{\text{data}}$ , a regularization penalty,  $\mathcal{L}_{\text{reg}}$ , and an optional boundary penalty,  $\mathcal{L}_{\text{bound}}$ . The total loss function is

$$\mathcal{L}_{\text{total}} = \mathcal{L}_{\text{data}} + \mathcal{L}_{\text{reg}} + \mathcal{L}_{\text{bound}}. \quad (5)$$

This aggregate loss is minimized via backpropagation, yielding a function  $\mathcal{N}$  that fits the absorbance data while adhering to prior knowledge about  $(\chi, T)$ . For comparison, this study also evaluates a conventional LAT algorithm based on Tikhonov regularization, with details provided in [Appendix A](#).

The data loss is based on the absorption spectroscopic model outlined in [Sec. 2.1](#),

$$\mathcal{L}_{\text{data}} = \frac{1}{|\mathcal{I} \times \mathcal{J} \times \mathcal{K}|} \sum_{i \in \mathcal{I}} \sum_{j \in \mathcal{J}} \sum_{k \in \mathcal{K}} \left\{ A_{k,i}(t_j) - \int_0^{L_i} K_k[\mathbf{r}_i(s), t_j] ds \right\}^2. \quad (6)$$

Here,  $A_{k,i}$  represents the absorbance of the  $k$ th transition measured by the  $i$ th laser at time  $t_j$ . The local absorption coefficient,  $K_k$ , is computed using Eqs. (2b) and (3), based on the  $\chi$  and  $T$  values predicted by  $\mathcal{N}$  at  $[\mathbf{r}_i(s), t_j]$ . The indicator function,  $\mathbf{r}_i$ , describes the path of the  $i$ th beam with a length  $L_i$ , while the integral in Eq. (6) is approximated at each training iteration using Monte Carlo sampling.

To implement this model for a given molecule, the line parameters for selected transitions of the target species are specified, and the necessary quantities are evaluated using the expressions above. The TIPS function is computed via linear interpolation of tabulated values provided in increments of 1 K [57]. To ensure numerical stability during backpropagation in single precision and to reduce floating-point operations, the constant terms in Eqs. (2b) and (3) are grouped together, and their products are precomputed.

## 2.3 Regularization Penalties

The network  $\mathcal{N}$  must possess sufficient expressivity to accurately represent the measured flow fields. While turbulent flows exhibit broadband frequency content, gradient-descent training of a coordinate neural network inherently introduces a low-frequency spectral bias. To mitigate this, we include a Fourier encoding (detailed in [Appendix B](#)) that enhances the network’s ability to represent broadband functions. However, a Fourier encoding can introduce random variations in  $\chi$  and  $T$  for limited-data beam arrays. Omitting the encoding, or using a smaller network, act as forms of implicit regularization: eliminating spurious high-frequency content but also inherently limiting the network’s ability to represent the true fields. Since implicit regularization often has unpredictable effects on the solution, it is preferable to retain  $\mathcal{N}$ ’s full capacity for capturing complex turbulent dynamics and instead incorporate explicit regularization, which imposes well-defined constraints with predictable outcomes to improve reconstruction accuracy.

In this work, we use a second-order Tikhonov penalty to produce smooth fields,

$$\mathcal{L}_g = \frac{1}{|\mathcal{A} \times \mathcal{T}|} \int_{\mathcal{T}} \int_{\mathcal{A}} \left\| \nabla^2 g \right\|_2^2 dx dt, \quad (7)$$

where  $\mathcal{T}$  represents the measurement interval,  $\mathcal{A}$  is the 2D or 3D RoI,  $\nabla^2$  is the spatial Laplacian operator,  $\|\cdot\|_2$  denotes the Euclidean norm, and  $g$  refers to an output of  $\mathcal{N}$  (either  $\chi$  or  $T$  in this case). Exact derivatives of the continuous field  $g$  are efficiently computed using automatic differentiation, and the integrals in Eq. (7) are approximated via Monte Carlo sampling. The regularization loss is defined as

$$\mathcal{L}_{\text{reg}} = \gamma_{\chi} \mathcal{L}_{\chi} + \gamma_T \mathcal{L}_T, \quad (8)$$

where  $\gamma_{\chi}$  and  $\gamma_T$  are weighting parameters. Selection of these parameters is discussed in the next section.

A boundary loss can be incorporated to account for known ambient conditions at the periphery of the measurement domain, ensuring the solution aligns with these conditions,

$$\mathcal{L}_{\text{bound}} = \frac{1}{|\partial\mathcal{A} \times \mathcal{T}|} \int_{\mathcal{T}} \int_{\partial\mathcal{A}} \gamma_{\text{bound},T} (T - T_0)^2 + \gamma_{\text{bound},\chi} (\chi - \chi_0)^2 dx dt. \quad (9)$$

In this expression,  $\partial\mathcal{A}$  denotes the boundary of the RoI and  $T_0$  and  $\chi_0$  are the known or estimated free-stream temperature and mole fraction, respectively. As in previous loss terms, these integrals are approximated using Monte Carlo sampling of the fields.

## 3 Parameter Selection

Proper selection of the regularization parameters in Eqs. (8) and (9) is crucial for accurate reconstruction [28]. For simplicity, consider the single-parameter case,

$$\mathcal{L}_{\text{total}} = \mathcal{L}_{\text{data}} + \gamma \mathcal{L}_{\text{reg}}. \quad (10)$$

Here,  $\gamma$  governs the trade-off between minimizing measurement residuals and promoting the physics-inspired properties encoded in  $\mathcal{L}_{\text{reg}}$ , like spatial smoothness. Small  $\gamma$  values lead to non-physical, least-squared solutions, while large values overweight the regularization term, often resulting in overly smooth or uniform fields, as observed with Tikhonov regularization. The optimal value balances these competing objectives, producing an estimate that closely approximates the true (unknown) field.

### 3.1 Classical Methods

Numerous techniques have been developed to optimize  $\gamma$ . Phantom studies involve generating synthetic data from CFD simulations of a representative flow or flame using the experimental beam layout. The data are corrupted with noise and reconstructed across various  $\gamma$  values; the optimal value is the one whose reconstructions best matches the simulated ground truth. While effective, this approach is often impractical due to the difficulty of accurately simulating a relevant phantom. Another method, the discrepancy principle, posits that the data loss,  $\mathcal{L}_{\text{data}}$ , should be of the same order of magnitude as the measurement noise variance [60]. However, this method often over regularizes solutions, resulting in smeared distributions [61]. Generalized cross-validation (GCV) selects the largest value of  $\gamma$  beyond which there is an inflection in the data loss, reflecting a trade-off between  $\mathcal{L}_{\text{data}}$  and  $\mathcal{L}_{\text{reg}}$  [62]. While widely used, GCV is numerically sensitive, making it challenging to reliably identify the optimal parameter [63].

The L-curve method provides a robust alternative. This approach involves plotting  $\mathcal{L}_{\text{reg}}$  against  $\mathcal{L}_{\text{data}}$  on logarithmic axes, forming an “L” shape. At small values of  $\gamma$ ,  $\mathcal{L}_{\text{data}}$  is minimized while  $\mathcal{L}_{\text{reg}}$  remains large, and the opposite is true at large  $\gamma$ . The optimal value corresponds to the point of maximum curvature, representing the best compromise between the two losses [28]. This point can be visually identified or computed through finite differences or a singular value analysis. Similar to the L-curve, Daun proposed a singular value approach for discrete linear problems in which  $\gamma$  is increased until the  $m$ th singular value of the aggregate operator, where  $m$  is the number of beams, begins to rise [23, 30]. Loosely speaking, this criterion confines the effect of regularization to the null space of the measurement operator. While the L-curve, GCV, and Daun’s method are conceptually related, the L-curve remains the most widely used parameter selection technique for LAT and is demonstrated for NILAT in Sec. 5.

### 3.2 Auto-Weighting Methods

A key challenge in regularization is the inconsistency between the regularization term,  $\mathcal{L}_{\text{reg}}$ , and the physics of the target process. True fields do not minimize  $\mathcal{L}_{\text{reg}}$ , except in trivial cases like uniform fields. As a result, regularization requires balancing two imperfect components: a data loss term, based on noisy measurements and an approximate operator, and a regularization term that does not fully align with the real system behavior. Adaptive weighting techniques, such as gradient-based [64, 65] and neural-tangent-kernel [66] methods, have been proposed for physics-informed neural networks (PINNs). These methods aim to ensure all loss terms contribute equally to parameter updates. In gradient-based auto-weighting, an objective loss of the form

$$\mathcal{L}_{\text{total}} = \sum_i \gamma_i \mathcal{L}_i \quad (11)$$

is periodically updated as follows:

$$\gamma'_i = \frac{\sum_j \|\nabla_{\theta} \mathcal{L}_j\|_2}{\|\nabla_{\theta} \mathcal{L}_i\|_2}, \quad (12)$$

where  $\nabla_{\theta}$  is the gradient operator with respect to the model parameters. Hence, training is accelerated for slowly-decreasing loss components and damped for rapidly-decreasing components. Smoothing is applied to the update,

$$\gamma_i^{(k+1)} = \beta \gamma_i^{(k)} + (1 - \beta) \gamma'_i, \quad (13)$$

where  $\beta$  is the smoothing parameter and  $\gamma_i^{(k)}$  is the weight after  $k$  iterations. This approach introduces three hyperparameters: the update frequency, smoothing factor, and initial  $\gamma_i$  values.

In tomographic applications like LAT,  $\mathcal{L}_{\text{data}}$  and  $\mathcal{L}_{\text{reg}}$  are fundamentally inconsistent. This is unlike PINNs, where evolution of the true fields is assumed to align with the equations included in the physics loss. The inconsistency of loss components in tomography raises questions about the effectiveness of auto-weighting for LAT (and particularly for NILAT). We compare the classical L-curve method with adaptive weighting in Sec. 5.2 to address this issue.

## 4 Case Studies

Four scenarios are analyzed in this work: one synthetic case and three experimental ones. The synthetic case is designed to mimic turbulent fluctuations and exhibit spectral content similar to the experimental scenarios, and it serves as a benchmark for evaluating NILAT. For the experimental cases, combustion products from three laboratory-scale burners are measured using a LAT sensor. Results from a conventional reconstruction algorithm are included in all cases to highlight the improved fidelity of NILAT, which performs nonlinear inversion for temperature and mole fraction in a single step, with direct regularization of the thermochemical state variables.

### 4.1 Synthetic Dataset

Significant advances in CFD have enhanced our understanding of reacting flows, but capturing all relevant scales of turbulent combustion while incorporating detailed chemical kinetics remains computationally intensive [67]. LAT algorithms are often benchmarked using Gaussian phantoms represented on coarse grids (typically with  $10^2$  to  $20^2$  elements) [10, 11, 23, 29]. While useful for evaluating reconstruction methods, these simplistic phantoms lack realistic features like recirculation zones, flame front wrinkling, and large oscillations that are characteristic of actual burners. To address this limitation, we designed an analytical

phantom with substantial spatio-temporal variations, inspired by the swirl burner studied by Liu et al. [18]. This burner sustains a crescent-shaped, precessing feature induced by the swirling inflow, which is a source of coherent unsteadiness.

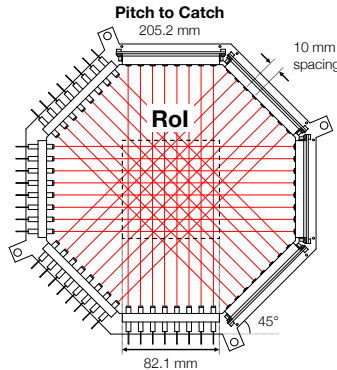


Figure 1: Schematic of the 32-beam LAT sensor used for the phantom study and experimental measurements.

The phantom fields are designed to capture realistic mean structures and spatio-temporal fluctuations, rather than replicate a specific flow. Figure 1 contains a schematic of the 32-beam LAT sensor and domain used for both our synthetic and experimental tests. The RoI is a central square with an 8.21 cm edge length, corresponding to the LAT beams’ common interrogation region. The sensor employs four banks of eight parallel beams, spaced 1 cm apart, with a 45° offset between banks [68]. The emitter and receiver units are separated by 20.52 cm. Two distributed feedback (DFB) lasers probe H<sub>2</sub>O transitions at 7185.59 cm<sup>-1</sup> and 7444.36 cm<sup>-1</sup>, chosen for their differential sensitivity across the anticipated temperature range [69]. Synthetic data are recorded at 250 Hz over a ten-second interval.

Both the phantom and NILAT estimates are continuous functions of  $\mathbf{x}$ , while the conventional algorithm represents the domain on a 40 × 40-pixel grid. All fields are presented on that grid for quantitative comparison. Phantoms are modeled as isobaric at 1 atm, with ambient conditions set to  $T = 306$  K and  $\chi_{\text{H}_2\text{O}} = 7.5 \times 10^{-3}$ . The ambient region outside the RoI is uniform, and variations in  $T$  and  $\chi$  are assumed to be perfectly correlated. Temperature and mole fraction fields are generated using circular Zernike polynomials [70, 71], fitted to distributions that mimic the combustion products of industrial and commercial burners. The mean fields have a toroidal structure, with peak values at the outer ring and lower values in the core, resembling a recirculation zone. Coherent temporal fluctuations are concentrated at the “flame front,” while incoherent spatio-temporal variations are distributed across the RoI. Z40 coefficients represent the mean and coherent components, with temporal oscillations modeled by a 9 Hz triangle-ramp function [70, 71]. This introduces a spectral peak at 9 Hz and maximum coherent fluctuations of 150 K in temperature and  $2.9 \times 10^{-3}$  in mole fraction. Pseudo-turbulence is generated with an additive Gaussian perturbation having a standard deviation of 2% of the largest Z40 coefficient. This methodology generates seemingly turbulent behavior with prominent fluctuations at the outer edge and a primary mode peaking at the prescribed frequency. The resulting phantom statistics align qualitatively with those observed in experimental flames, as shown in Sec. 5.3.2

From these temporally varying fields, high-fidelity absorbance signals are generated using line parameters and TIPS functions from HITRAN2020 [57, 58]. Absorbances are computed using Eq. (2a), with the spatial integral approximated by sampling points along each line of sight between the emitter and receiver units. Pink additive noise with a standard deviation of 1% of  $\max(A_k)$  is added to the projection data to simulate realistic LAT imaging conditions. This noise level corresponds to an SNR of 40 dB, which is representative of laboratory or well-controlled industrial environments.

## 4.2 Experimental Datasets

We experimentally demonstrate NILAT on a set of laboratory-scale burners, shown in Fig. 2, designed to test its ability to recover flow features that are common in industrial and commercial settings. From left to right in Fig. 2: (1) the “round burner” has a 4.1 cm cap with closely spaced outlets across most of its

surface, except for a small central region, producing a single round plume of combustion products; (2) the “annular burner” features a 5.1 cm cap with outlets distributed across a sloping surface, having inner and outer diameters of 3.1 and 5.1 cm, generating a ring of flames; and (3) the “triple burner” comprises three 2.6 cm caps with evenly spaced outlets, arranged in a triangular formation with a center-to-center spacing of 3.2 cm, producing three hot spots. The burners are fueled by propane at flow rates of 1.485, 1.099, and 1.103 L/min for the round, annular, and triple burners, respectively. Some air is entrained upstream of the outlets, resulting in a combination of partially- and non-premixed combustion.

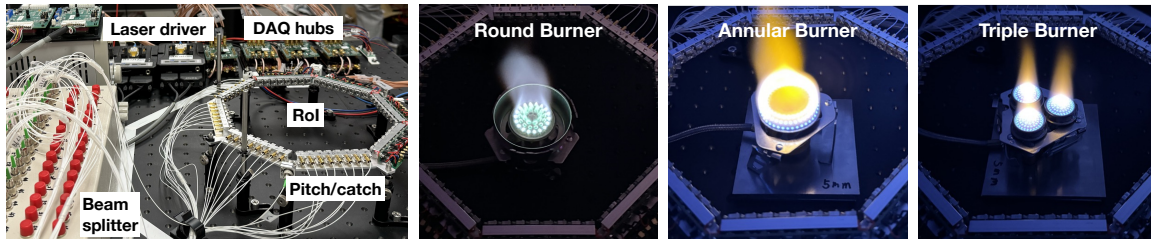


Figure 2: LAT sensor and data acquisition system (left) used to probe three commercially available burners (right).

The LAT sensor geometry and RoI selection match the setup described in Sec. 4.1. Measurements are taken at planes located 3 mm above the round and triple burners and 7 mm above the annular burner. Each DFB laser diode (NTT Electronics NLK1E5GAAA, NLK1B5GAAA) is temperature- and current-controlled by a laser driver (Wavelength Electronics LDTC 2-2E). Wavelength modulation is performed at a 1 kHz scan rate, with the  $7185.59\text{ cm}^{-1}$  and  $7444.36\text{ cm}^{-1}$  lasers multiplexed in the frequency domain using sinusoidal modulations at 100 kHz and 130 kHz, respectively. Each laser beam is collected by a photodiode, trans-impedance amplified, and digitized with 16-bit resolution at 15.625 Msps. All channels are synchronized by an external trigger and 4-to-1 time-division-multiplexed across neighboring scans, yielding an imaging rate of 250 Hz [72, 73]. Path-integrated absorbances,  $A_k$ , as defined in Eq. (2a), are calculated for each scan and beam by fitting the  $2f/1f$  signal using a Voigt profile, where  $A_k$  corresponds to the area parameter [74]. Measurements span a ten-second interval, during which the flames burn continuously at fixed propane flow rates. Following the LAT measurements, an S-type thermocouple is used to probe average temperatures at selected points above each burner. While these thermocouple measurements are intrusive and biased by radiative heating of the probe, they provide a useful baseline to gauge the accuracy of our reconstructions.

## 5 Tomographic Reconstructions and Analysis

### 5.1 Implementation

Neural reconstructions were implemented in PyTorch 2.0.1 using a network architecture with five hidden layers, each containing 250 nodes. Weights were initialized from a standard normal distribution, and biases were set to zero. Reconstructions were performed with the Adam optimizer over 80 epochs at a learning rate of  $10^{-3}$ , followed by a refinement stage of four epochs at  $10^{-4}$ . NILAT reconstructions encompassed the full octagonal sensing area, with ambient conditions weakly enforced on  $\partial\mathcal{A}$  via the boundary loss in Eq. (9). The boundary was dynamically estimated as the largest ellipse defined by beams that did not intersect the hot products. Batch sizes were set to include all beams at five time instances for  $\mathcal{L}_{\text{data}}$ , 10,000 interior points for  $\mathcal{L}_{\text{penalty}}$ , and 10,000 ambient points for  $\mathcal{L}_{\text{bound}}$ . Absorbances were computed for each beam using 2000 random points along the path, yielding a standard deviation below 2% of the long-run value.

Conventional reconstructions were computed as a baseline for comparison. For the two-step linear algorithm detailed in Appendix A, the RoI was discretized into a  $40 \times 40$ -pixel grid, with uniform conditions applied outside the RoI. These ambient parameters,  $(T_0, \chi_0)$ , were optimized during the reconstruction. Local absorption coefficient fields,  $K_k$ , for the  $7185\text{ cm}^{-1}$  and  $7444\text{ cm}^{-1}$  transitions were reconstructed using second-order Tikhonov regularization, and the linear system was solved by a non-negative least squares optimization algorithm. Optimal regularization parameters were determined through an L-curve analysis, selecting the point of maximum curvature for each dataset. Reconstructed  $(K_1, K_2)$  values were converted



to  $(T, \chi)$  at each pixel through radiometric thermometry [75].

The reconstructed fields were analyzed using statistical methods and spectral proper orthogonal decomposition (SPOD) [76]. SPOD decomposes time-varying data into orthogonal modes ranked by energy, providing eigenvalues and spatial eigenvectors at selected frequencies to capture coherent spatio-temporal content in the dataset. In this work, SPOD was applied to the time-resolved temperature field estimates. Each analysis included all 2500 snapshots, which were recorded at 250 Hz. We used blocks of 250 time instances with 50% overlap for SPOD, resulting in 19 blocks and a frequency resolution of 1 Hz.

## 5.2 Phantom Study Results

We begin by analyzing the results of our phantom study, focusing on the use of an L-curve to approximate the optimal regularization parameter. For simplicity, the regularization losses are weighted with a single parameter,  $\gamma = \gamma_T = \gamma_\chi$ , which assumes proper normalization of  $\mathcal{L}_T$  and  $\mathcal{L}_\chi$  by a representative variance. The boundary losses,  $\gamma_{\text{bound},T}$  and  $\gamma_{\text{bound},\chi}$ , are easily satisfied when set above a minimal threshold.<sup>4</sup> As a result, optimizing  $\gamma$  in NILAT reduces to selecting an appropriate value for the single regularization parameter in Eq. (10).

### 5.2.1 Parameter Selection Methods

To explore this, we reconstructed the phantom using  $\gamma$  values ranging from  $10^{-13}$  to  $10^{-4}$ . The leftmost plot in Fig. 3 illustrates the training progression for each  $\gamma$ . At the outset, the randomly-initialized networks yield large values of  $\mathcal{L}_{\text{data}}$  and  $\mathcal{L}_{\text{reg}}$ , placing them towards the upper-right corner of the plot. During training, the networks progress leftward and downward, as both losses are minimized, and converge to their respective terminus on the L-curve. Sample reconstructions of  $T$  are shown for several values of  $\gamma$  along the bottom of Fig. 3. The right plot in Fig. 3 shows reconstruction errors for  $T$  and  $\chi$  as functions of  $\gamma$ , revealing similar behavior for both fields, which supports the use of a single regularization parameter, i.e., since there is no trade-off between the accuracy of  $T$  and  $\chi$ . Reconstruction errors are minimized near  $\gamma = 10^{-8}$ , aligning with the region of maximum curvature at the bend of the L-curve. Moreover, the basin of low error extends from roughly  $\gamma = 10^{-8}$  to  $10^{-7}$ , so there is some flexibility in the selection of  $\gamma$ . In cases where the reconstructed fields exhibit distinct behaviors, such as significantly different energy spectra, it may be necessary to optimize multiple regularization parameters, e.g.,  $\gamma_T$  and  $\gamma_\chi$ .

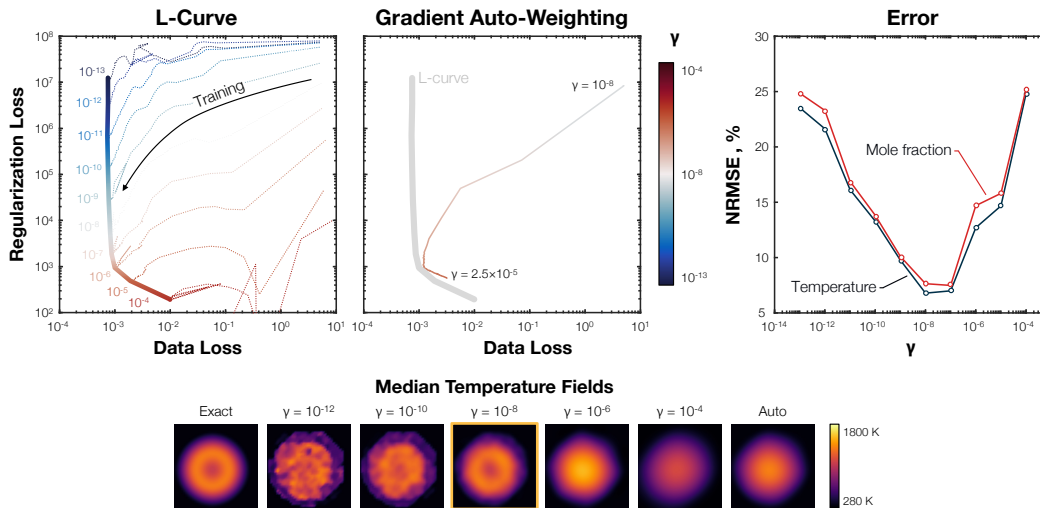


Figure 3: (Top row) Reconstructions at various  $\gamma$  values form an L-curve (left); the gradient-based auto-weighted trajectory initially approaches the optimal value but diverges with continued training (center). Minimum errors align with the point of maximum curvature on the L-curve (right). (Bottom row) Sample reconstructions for different  $\gamma$  values and the auto-weighted trajectory.

In addition to L-curve analysis, we evaluated the gradient auto-weighting technique proposed by Wang et al. for PINNs, as detailed in Sec. 3.2. The central plot in Fig. 3 compares an auto-weighted trajectory

<sup>4</sup>Our results were invariant to the selection of  $\gamma_{\text{bound},T}$  and  $\gamma_{\text{bound},\chi}$  across four orders of magnitude.

with the L-curve, using an update frequency of 500 iterations, a smoothing factor of  $\beta = 0.9$ , and an initial  $\gamma$  determined from a prior L-curve analysis ( $\gamma = 10^{-8}$ ). While the auto-weighted trajectory initially approached the L-curve’s point of maximum curvature, it diverged with continued training, bending toward the high- $\gamma$  leg. This behavior was observed across all tested hyperparameter settings and produced overly-smooth reconstructions, as shown in the bottom row of Fig. 3. Divergence occurs because the magnitude of gradients of the regularization term,  $\nabla_{\theta} \mathcal{L}_{\text{reg}}$ , diminishes more rapidly than that of the data fidelity term,  $\nabla_{\theta} \mathcal{L}_{\text{data}}$ . Smooth fields are inherently easier for the network to generate than fields consistent with the absorbance measurements, which drives repeated increases in  $\gamma$ . These increases progressively prioritize the regularization penalty, causing training to focus on minimizing  $\mathcal{L}_{\text{reg}}$ , further reducing the magnitude of  $\nabla_{\theta} \mathcal{L}_{\text{reg}}$ . This creates a feedback loop that amplifies the emphasis on regularization while neglecting the data fidelity term, ultimately leading to suboptimal reconstructions. While this issue is less problematic in settings with consistent loss terms, it poses a challenge in tomographic applications where the loss components are inherently inconsistent. Gradient-based auto-weighting tends to disproportionately minimize one (inconsistent) loss component over the others, leading to imbalanced solutions. These findings suggest that traditional methods like the L-curve remain preferable for selecting  $\gamma$  in tomographic applications.

### 5.2.2 Hysteresis Effects

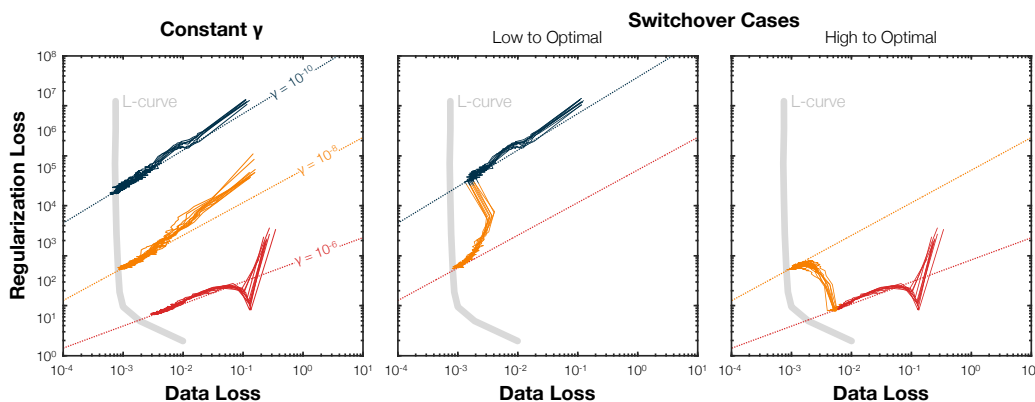


Figure 4: Training trajectories for ensembles of networks show similar endpoints under fixed  $\gamma$  values (left). Networks quickly adapt to new  $\gamma$  trajectories following a switch (middle, right).

Another important finding is that NILAT does not exhibit hysteresis effects during training, meaning the process is not path-dependent and converges to a consistent optimum. This property simplifies the application of classical parameter selection methods like the L-curve. To test this, we trained networks with and without switching  $\gamma$  halfway through optimization. Results are shown in Fig. 4. For each condition, an ensemble of ten networks was trained using one of three initial  $\gamma$  values:  $10^{-10}$ ,  $10^{-8}$  (near the optimal value), or  $10^{-6}$ . In the left plot of Fig. 4,  $\gamma$  was held constant during training, while in the middle and right plots,  $\gamma$  was switched midway from  $10^{-10}$  to  $10^{-8}$  and from  $10^{-6}$  to  $10^{-8}$ , respectively. In the latter cases, the networks quickly adjusted to the new  $\gamma$  trajectory, following the corresponding path towards the terminus for  $\gamma = 10^{-8}$ . This behavior demonstrates that NILAT responds predictably to changes in  $\gamma$ , further supporting its compatibility with L-curve analysis and other classical parameter selection techniques.

### 5.2.3 Assessing Reconstructions

Figure 5 compares the median temperature and  $\text{H}_2\text{O}$  mole fraction fields of the ground truth phantom, conventional reconstruction, and NILAT reconstruction. NILAT accurately recovers the toroidal structure of the phantom, with peak amplitudes closely matching those of the true fields. In contrast, the conventional reconstruction fails to resolve key features, most notably the cool pseudo-recirculation zone in the center of the phantom is entirely absent. This shortcoming is critical, as it can lead to misinterpretations of burner dynamics. Vertical cut plots of the temperature field, shown in Fig. 6, further illustrate this point, displaying the median profiles and  $2\sigma$  ranges for the ground truth, NILAT reconstruction, and conventional LAT reconstruction. NILAT effectively reproduces the true median profile and captures the fluctuations well, although it slightly underpredicts the variance of  $T$  on one side of the phantom. This underprediction stems

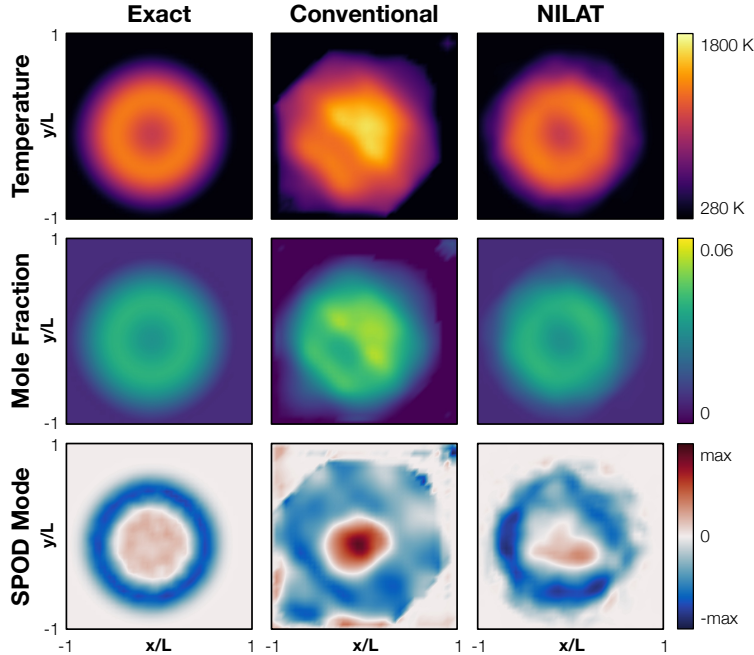


Figure 5: Reconstructions of the phantom: ground truth (left column), conventional reconstructions (middle column), and NILAT reconstructions (right column). Rows correspond to temperature (top),  $\chi_{\text{H}_2\text{O}}$  (middle), and the leading SPOD mode (bottom).

from challenges in recovering small, fluctuating features with a limited number of beams. The conventional reconstructions, however, exhibit wild, non-physical oscillations that are hundreds of degrees larger than the true values.

The ability of NILAT to resolve temporal dynamics is further demonstrated through SPOD modes. The first SPOD mode at the dominant frequency of 9 Hz, which contains nearly all the coherent energy in this phantom, is presented in the bottom-left corner of Fig. 5. This mode features oscillations along the outer edge (the “flame front”) paired with weaker, inversely correlated fluctuations at the center. NILAT recovers the mode’s spatial structure remarkably well, even with the limited 32-beam data, and the magnitude of this mode is accurately estimated in the reconstructed time series. This result highlights NILAT’s potential to reveal reacting flow dynamics in optically restricted environments, such as high-pressure burners or production pistons. In contrast, the conventional algorithm produces a distorted SPOD mode, with an enlarged outer ring, a compressed core, and overly sharp gradients, resulting in an inaccurate representation of the flow. Moreover, the magnitudes of fluctuations associated with this mode are significantly overestimated in the reconstructions. Overall, we find NILAT is suitable for reconstructing both steady-state profiles and transient, coherent dynamics, offering significant advantages for analyzing complex reacting flows over contemporary algorithms for LAT.

### 5.3 Experimental Reconstructions and Analysis

We further demonstrate the applicability and advantages of NILAT through experimental measurements of the three reacting flows described in Sec. 4.2. Our analysis begins with qualitative and quantitative evaluations of the average reconstructions, followed by a discussion of unsteadiness and the improved accuracy achieved with NILAT.

#### 5.3.1 Mean Reconstructions

Figure 7 presents the median temperature and  $\text{H}_2\text{O}$  mole fraction fields for all three burners. The left columns show results from the conventional LAT algorithm, while the right columns display NILAT reconstructions. Both methods capture the general structure of the products, including the ring of hot water vapor above each burner cap, enclosing a slightly cooler core with a lower concentration of water vapor. These cooler zones become more pronounced with larger burner caps. NILAT provides a far clearer rep-

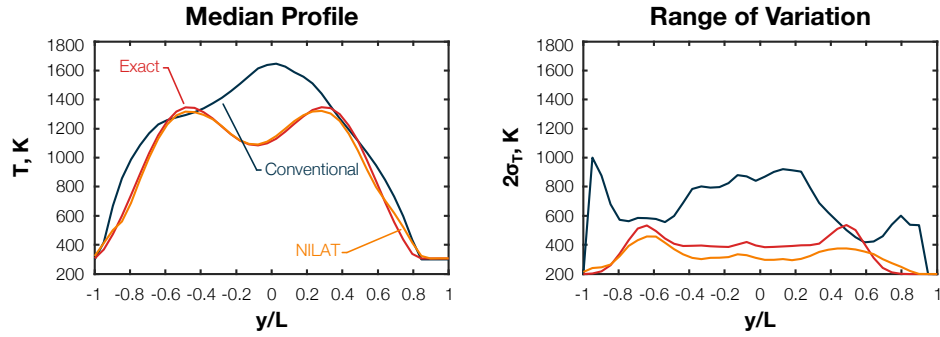


Figure 6: Temperature profiles for the phantom: peak magnitudes and structure match the ground truth (left). Ranges of variation (right) are well-matched by NILAT, whereas conventional reconstructions exhibit non-physical ranges.

resentation of these structures, better capturing the expected strong correlation between  $T$  and  $\chi_{\text{H}_2\text{O}}$  and producing reconstructions with well defined plume shapes. In contrast, conventional LAT reconstructions severely overestimate the spatial extent of the hot products, resulting in diffuse fields that lack critical flow / combustion features and are marked by artifacts.

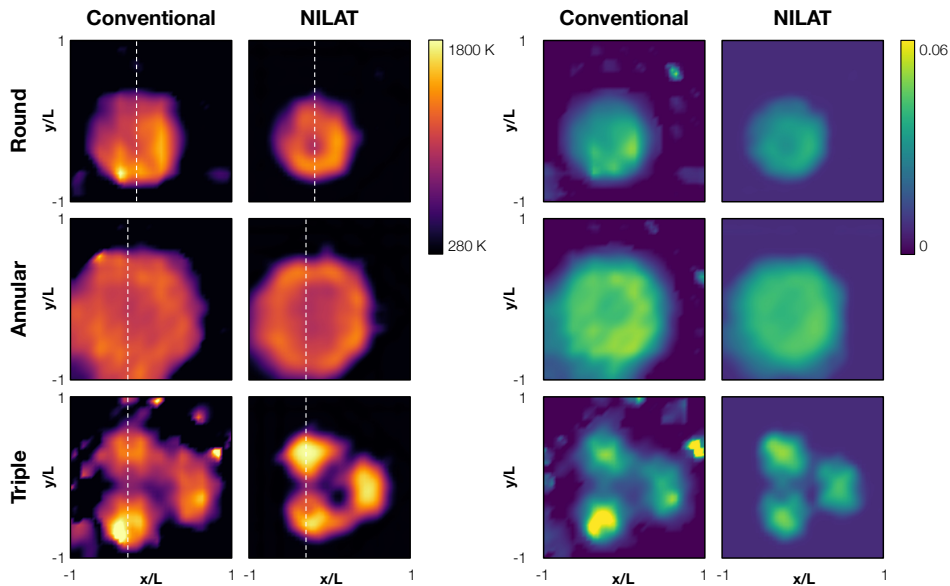


Figure 7: Median temperature and  $\chi_{\text{H}_2\text{O}}$  distributions for three experimental burner configurations. Dashed lines indicate locations of profile cuts.

One-dimensional cut plots of the temperature fields from Fig. 7 are presented in Fig. 8. These cuts show-case differences between the reconstructed temperature profiles above each burner. The top row depicts median temperature profiles over the time series, while the bottom row shows the  $2\sigma$  range, highlighting the major non-physical fluctuations produced by the conventional algorithm. Dashed lines in the median plots indicate the highest (time-averaged) temperatures recorded in our thermocouple measurements. NILAT reconstructions exhibit better agreement with the thermocouple measurements than the conventional LAT algorithm. Additionally, NILAT captures spatial features such as the central cold zone in the round and annular burners and the symmetry between sub-burners in the triple configuration with greater accuracy, indicating its superior spatial resolution.

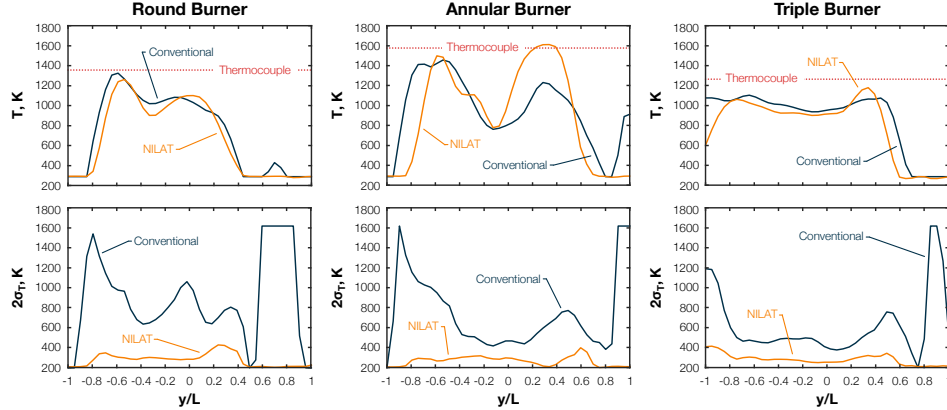


Figure 8: Temperature profiles and ranges of variation for the three experimental burners. NILAT reconstructions are sharper and exhibit reasonable unsteadiness profiles compared to the erratic profiles from the conventional reconstructions.

### 5.3.2 Instantaneous and Modal Results

Time-resolved measurements of unsteady flames provide valuable insights into coupled flow and combustion mechanisms. Power spectral density (PSD) plots in Fig. 9 show dominant tonal frequencies of 14 Hz, 9 Hz, and 9 Hz for the round burner, annular burner, and synthetic phantom, respectively. The phantom’s tone was deliberately introduced to mimic experimental dynamics, while the triple burner displayed broadband fluctuations without any significant tones. The similarity between the synthetic and experimental absorbance data supports the phantom’s relevance to realistic conditions.

Spectral analysis of the reconstructed flow fields from the round and annular burners reveals NILAT’s ability to capture coherent dynamics of these burners. SPOD modes at the dominant frequencies derived from NILAT reconstructions reveal cyclical oscillations at the plume’s periphery, with peripheral fluctuations negatively correlated to inner fluctuations. These structures are indicative of flame flickering, a buoyancy-driven instability common in low-speed non-premixed flames. In contrast, modes derived from conventional LAT reconstructions are incoherent and spatially diffuse, failing to resolve this dynamic. Flame flickering arises from buoyancy-induced vortices formed near the base of the flame, produced by Kelvin–Helmholtz instabilities in the shear layer [77]. These vortices entrain cooler ambient air into the reaction zone at the edge of the plume, enhancing the reaction rate locally and causing a localized outward propagation of the reaction front. Cyclic entrainment and enhanced-reaction events drive the characteristic expansion and contraction of the flame. NILAT accurately resolves this progression, capturing the oscillations at the plume’s periphery and within its center, which are essential for understanding flame behavior in such configurations.

Time-resolved reconstructions, provided in the supplementary material, further illustrate NILAT’s ability to recover both large- and small-scale features of the target flows. These results demonstrate the method’s robustness and potential for analyzing unsteady combustion phenomena in optically restricted environments.

## 6 Conclusions

This paper introduces *NILAT*: a nonlinear, neural-implicit reconstruction algorithm for laser absorption tomography that reconstructs  $2D + t$  distributions of temperature and targeted partial pressures from absorbance data. By embedding line parameters and TIPS functions into a nonlinear measurement operator, *NILAT* performs direct reconstruction and regularization on the physical quantities of interest ( $T, \chi, p$ , etc.) rather than absorption coefficient fields. The space–time formulation supports both explicit and implicit regularization of temporal dynamics and facilitates comprehensive data assimilation. Additionally, the neural framework provides significant data compression, enabling scalability to higher spatial resolutions, longer time horizons, larger beam arrays, and multi-transition absorption setups.

The performance of *NILAT* was validated through a phantom study, where it successfully captured large-scale features of the phantom and its dynamics using a sparse imaging array. The algorithm ac-

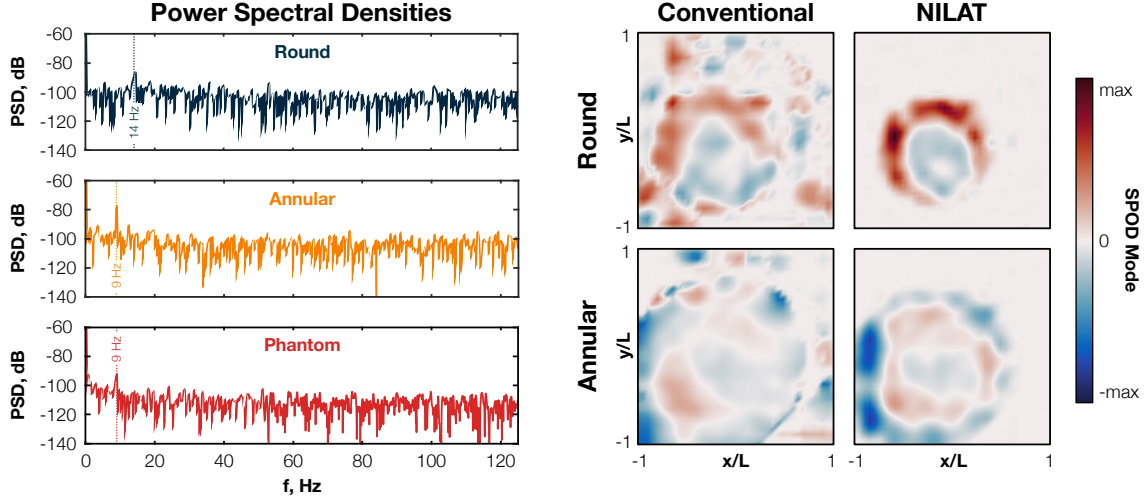


Figure 9: PSDs (left) and SPOD modes (right) for the round and annular burners. The spectral peaks correspond to coherent oscillations near the flame front, which are anti-correlated with weaker central fluctuations.

curately reconstructed both the toroidal temperature and water vapor mole fraction structures and the dominant temperature SPOD mode, demonstrating high-fidelity tomographic imaging. NILAT’s robustness to hysteresis ensures compatibility with classical parameter selection techniques like L-curve analysis. Conversely, gradient auto-weighting proved unsuitable for LAT, as the inconsistency between data and regularization loss terms led to overly smoothed solutions, a limitation not observed in PINNs, where the technique originated.

Experimental reconstructions using three burners further showcased NILAT’s advantages. The algorithm faithfully recovered large-scale flow structures, significantly reduced artifacts, and achieved quantitative agreement with thermocouple measurements. It also effectively captured dominant flame dynamics, such as flickering, with SPOD modes consistent with our expectations for non-premixed flames. These findings demonstrate NILAT’s potential to advance LAT applications. Future research will extend NILAT to multi-species imaging and explore its application to absorption-based velocimetry scenarios.

## Appendix A Discrete Laser Absorption Tomography

The conventional approach to LAT begins with a vector of absorbance data in  $\mathbb{R}^m$ ,

$$\mathbf{a}_k = (A_{k,1}, A_{k,2}, \dots, A_{k,m}). \quad (14)$$

Instead of using a coordinate-based neural network, field variables are represented with a finite basis of  $n$  functions,  $\{\varphi_1, \varphi_2, \dots, \varphi_n\}$ . In this work, we employ a 2D pixel basis, where the basis function  $\varphi_j$  is unity inside the  $j$ th pixel and zero outside. An arbitrary field variable,  $g$ , is then approximated as:

$$g(\mathbf{x}) = \sum_{j=1}^n g_j \varphi_j(\mathbf{x}), \quad (15)$$

where  $g_j$  is the coefficient for the  $j$ th basis function, and  $g$  represent variables such as  $\chi$ ,  $T$ , or  $K_k$ . Field variables are thus represented by vectors of  $n$  coefficients,

$$\boldsymbol{\chi} = (\chi_1, \chi_2, \dots, \chi_n), \quad (16a)$$

$$\mathbf{T} = (T_1, T_2, \dots, T_n), \quad \text{and} \quad (16b)$$

$$\mathbf{k}_k = (K_{k,1}, K_{k,2}, \dots, K_{k,n}), \quad (16c)$$

where elements of  $\mathbf{k}_k$  are computed using corresponding values in  $\boldsymbol{\chi}$  and  $\mathbf{T}$  via Eq. (2b) for each  $k \in \mathcal{K}$ .

The integrated absorbance model for the  $i$ th beam can be approximated using the finite basis introduced above,

$$A_{k,i} = \int_0^{L_i} K_k[\mathbf{r}_i(s)] ds \approx \int_0^{L_i} \sum_{j=1}^n K_{k,j} \varphi_j[\mathbf{r}_i(s)] ds = \sum_{j=1}^n K_{k,j} \underbrace{\int_0^{L_i} \varphi_j[\mathbf{r}_i(s)] ds}_{W_{i,j} \equiv \frac{\partial A_{k,i}}{\partial K_{k,j}}} \quad (17)$$

where  $W_{i,j}$  is the sensitivity of the  $i$ th absorbance measurement to the spectral absorption coefficient in the  $j$ th pixel. For a pixel basis,  $W_{i,j}$  is simply the chord length of the  $i$ th beam within the  $j$ th pixel. Given an  $m \times 1$  data vector,  $\mathbf{a}_k$ , spectrally integrated LAT for a single transition (a.k.a. monochromatic LAT), is a linear inverse problem,

$$\mathbf{a}_k = \mathbf{W}\mathbf{k}_k, \quad (18)$$

where  $\mathbf{a}_k$  is measured and  $\mathbf{k}_k$  must be inferred. This equation admits an infinite set of solutions when the column rank of  $\mathbf{W}$  is less than  $m$ , which is guaranteed when  $m < n$ , as is almost always the case in LAT.

### Appendix A.1 Linear Reconstruction with Spectroscopic Post-Processing

In the linear approach to LAT, Eq. (18) is inverted for each measured wavenumber or transition. The resulting values of  $\mathbf{k}_k$  for  $k \in \mathcal{K}$  are used to estimate the state variables at each basis function. While numerous regularization techniques exist, we focus here on one of the most common methods: second-order Tikhonov regularization. This approach involves the minimization

$$\hat{\mathbf{k}}_k = \arg \min_{\mathbf{k}_k} \|\mathbf{a}_k - \mathbf{W}\mathbf{k}_k\|_2^2 + \gamma^2 \|\mathbf{L}\mathbf{k}_k\|_2^2, \quad (19)$$

where  $\mathbf{L}$  is the discrete Laplacian. Minimizing  $\|\mathbf{L}\mathbf{k}_k\|_2^2$  together with the data fidelity term  $\|\mathbf{a}_k - \mathbf{W}\mathbf{k}_k\|_2^2$  promotes smooth solutions with small second derivatives. This regularization method is computationally efficient and generally produces reasonable results, but it lacks a direct connection to the spatial derivatives of  $\chi$  and  $T$ .

For spectrally integrated data, local Boltzmann plots are used to determine  $\chi$  and  $T$ . These plots incorporate reconstructed absorption coefficient values and line parameters,

$$y_B = \log \underbrace{\left[ \frac{K_k}{S_{\text{ref},k}} \exp\left(\frac{c_2 E_k''}{T_{\text{ref}}}\right) \right]}_{\text{measured and plotted}} = \underbrace{\frac{-c_2 E_k''}{T} + \log \left[ \frac{\chi p}{k_B T} \frac{Q(T_{\text{ref}})}{Q(T)} \right]}_{\text{unknown } \{\chi, T, p\}} \quad (20a)$$

$$x_B = c_2 E_k'', \quad (20b)$$

where each transition at each basis function (pixel) provides one  $(x_B, y_B)$  point.<sup>5</sup> Using this definition,

$$T = - \left( \frac{dy_B}{dx_B} \right)^{-1} \quad (21a)$$

and

$$\chi = \frac{k_B T}{p} \frac{Q(T)}{Q(T_{\text{ref}})} \exp\left(\frac{c_2 E_k''}{T}\right). \quad (21b)$$

These expressions are evaluated at each pixel, and accuracy improves with increasing spectral information. This approach reduces to ratio thermometry when only two transitions are available. In the spectrally-resolved case, the local thermochemical state is determined through regression, as described in [12].

<sup>5</sup>The simplified expression for  $y_B$  is obtained by substituting Eqs. (2b) and (3) into Eq. (20a), assuming that  $c_2 \nu_k \ll 1$ , which is reasonable at the wavenumbers and temperatures considered in this work.

## Appendix A.2 Spectrally Integrated Nonlinear Reconstruction

The nonlinear LAT reconstruction problem with second-order Tikhonov regularization for the mole fraction and temperature fields corresponds to the following minimization:

$$(\hat{\chi}, \hat{\mathbf{T}}) = \arg \min_{(\chi, \mathbf{T})} \sum_{k \in \mathcal{K}} \|\mathbf{a}_k - \mathbf{W} \mathbf{k}_k(\chi, \mathbf{T})\|_2^2 + \gamma_\chi^2 \|\mathbf{L}\chi\|_2^2 + \gamma_{\mathbf{T}}^2 \|\mathbf{L}\mathbf{T}\|_2^2, \quad (22)$$

which can be solved using a variety of optimization techniques [78]. Note that we have not introduced any time dependencies in our presentation of the conventional LAT problem. While it is possible to perform space–time reconstructions using a discrete formulation, the dimensions of  $\chi$  and  $\mathbf{T}$  increase linearly with the number of time steps, resulting in very large matrix systems. In contrast,  $\mathcal{N}$  offers a highly compressed representation of  $(\chi, T)$ , making it well-suited for long datasets.

## Appendix B Network Architecture

Flow fields are represented using a coordinate-based neural network with an input layer, output layer, and  $n_1$  hidden layers,

$$\mathcal{N}(\mathbf{z}^0) = \sigma_{\text{sig}} \left\{ \mathbf{W}^{n_1+1} \left[ \mathcal{G}^{n_1} \circ \mathcal{G}^{n_1-1} \circ \dots \circ \mathcal{G}^2 \circ \mathcal{F}(\mathbf{z}^0) \right] + \mathbf{b}^{n_1+1} \right\}, \quad (23a)$$

with

$$\mathbf{z}^l = \mathcal{G}^l(\mathbf{z}^{l-1}) = \sigma_{\text{swish}}(\mathbf{W}^l \mathbf{z}^{l-1} + \mathbf{b}^l) \quad \text{for } l \in \{2, 3, \dots, n_1\}. \quad (23b)$$

The vector  $\mathbf{z}^l$  contains the values of neurons in the  $l$ th layer,  $\mathbf{W}^l$  and  $\mathbf{b}^l$  are the weight matrix and bias vector for the  $l$ th layer, and  $\sigma$  is a nonlinear activation function that is applied to each element of the argument. The vector  $\theta$  contains all the trainable weights and biases in  $\mathcal{N}$ . We use swish activation functions in the hidden layers for stability during backpropagation, and we apply a sigmoid function at the final layer to bound outputs to physically reasonable ranges:  $280 \text{ K} \leq T < 1800 \text{ K}$  and  $0.0075 \leq \chi < 0.053$ . These bounds improve convergence and can be adjusted based on the sensing scenario.

To address the ‘‘spectral bias’’ of vanilla MLPs, which limits their ability to represent high-frequency details, we replace the first hidden layer with a Fourier encoding,

$$\mathbf{z}^1 = \mathcal{F}(\mathbf{z}^0) = \left[ \sin(2\pi\omega_1 \cdot \mathbf{z}^0), \cos(2\pi\omega_1 \cdot \mathbf{z}^0), \dots, \sin(2\pi\omega_w \cdot \mathbf{z}^0), \cos(2\pi\omega_w \cdot \mathbf{z}^0) \right]. \quad (24)$$

Here,  $w$  is the number of Fourier features, and  $\omega$  contains random frequencies sampled from a normal distribution. Separate spatial and temporal standard deviations ensure the basis spans all anticipated space–time frequencies [79]. Inputs are normalized by the sensor’s maximum length and the dataset’s acquisition time. Outputs are range-normalized and scaled to dimensional form during evaluations. Regularization losses are computed in non-dimensional form to enhance algorithmic stability.

## Novelty and Significance Statement

Gas turbine combustors pose significant challenges for diagnostics due to their harsh operating conditions and minimal optical access. This work presents the first demonstration of simultaneous, long-time horizon reconstructions of 2D temperature and water vapor mole fraction fields in laboratory burners using neural-implicit laser absorption tomography (NILAT). We characterize NILAT through a phantom study that features a realistic mean profile, broadband fluctuations, and tonal dynamics, highlighting its robustness and accuracy. Additionally, we validate the utility of established parameter selection methodologies and explore the use of deep ensembles for uncertainty quantification. This sensing methodology extends beyond laboratory conditions and has the potential for application in other extreme environments where direct measurements are infeasible.

## Declaration of Competing Interests

The authors declare that they have no known competing financial interests or personal relationships that could have appeared to influence the work reported in this paper.



## Acknowledgments

C.L. acknowledges support from the EPSRC through Programme Grant EP/T012595/1, Platform Grant EP/P001661/1, and Impact Acceleration Account PV120. S.J.G. acknowledges support from NASA under contract 80NSCC24PB449 and from FAU Erlangen-Nürnberg. J.P.M. acknowledges support from the DoD through an NDSEG Fellowship.

## References

- [1] A. M. Steinberg, P. E. Hamlington, and X. Zhao, "Structure and dynamics of highly turbulent premixed combustion," *Prog. Energy Combust. Sci.* **85**, 100900 (2021).
- [2] M. Stöhr, I. Boxx, C. D. Carter, and W. Meier, "Experimental study of vortex-flame interaction in a gas turbine model combustor," *Combust. Flame* **159**, 2636–2649 (2012).
- [3] C. C. Rasmussen, S. K. Dhanuka, and J. F. Driscoll, "Visualization of flameholding mechanisms in a supersonic combustor using PLIF," *Proc. Combust. Inst.* **31**, 2505–2512 (2007).
- [4] C. Schulz, V. Sick, J. Wolfrum, V. Drewes, and R. Maly, "Quantitative 2D single-shot imaging of NO concentrations and temperatures in a transparent SI engine," in "Symp. (Int.) Combust.", , vol. 26 (Elsevier, 1996), vol. 26, pp. 2597–2604.
- [5] S. W. Powers, G. Byun, and K. T. Lowe, "Validation of filtered Rayleigh scattering optical rake measurement techniques in turbomachinery applications and boundary layers," *J. Turbomach.* **146** (2024).
- [6] S. J. Beresh, "Time-resolved particle image velocimetry," *Meas. Sci. Technol.* **32**, 102003 (2021).
- [7] F. Scarano, "Tomographic PIV: principles and practice," *Meas. Sci. Technol.* **24**, 012001 (2012).
- [8] A. Schröder and D. Schanz, "3D Lagrangian particle tracking in fluid mechanics," *Annu. Rev. Fluid Mech.* **55**, 511–540 (2023).
- [9] M. Altenhoff, S. Aßmann, J. F. Perlitz, F. J. T. Huber, and S. Will, "Soot aggregate sizing in an extended premixed flame by high-resolution two-dimensional multi-angle light scattering (2D-MALS)," *Appl. Phys. B* **125**, 1–15 (2019).
- [10] W. Cai and C. F. Kaminski, "Tomographic absorption spectroscopy for the study of gas dynamics and reactive flows," *Prog. Energy Combust. Sci.* **59**, 1–31 (2017).
- [11] C. Liu and L. Xu, "Laser absorption spectroscopy for combustion diagnosis in reactive flows: A review," *Appl. Spectrosc. Rev.* **54**, 1–44 (2019).
- [12] S. J. Grauer, J. Emmert, S. T. Sanders, S. Wagner, and K. J. Daun, "Multiparameter gas sensing with linear hyperspectral absorption tomography," *Meas. Sci. Technol.* **30**, 105401 (2019).
- [13] Q. Qu, Z. Cao, L. Xu, C. Liu, L. Chang, and H. McCann, "Reconstruction of two-dimensional velocity distribution in scramjet by laser absorption spectroscopy tomography," *Appl. Opt.* **58**, 205–212 (2018).
- [14] S. J. Grauer and A. M. Steinberg, "Linear absorption tomography with velocimetry (LATV) for multi-parameter measurements in high-speed flows," *Opt. Express* **28**, 32676–32692 (2020).
- [15] P. Wright, N. Terzija, J. L. Davidson, S. Garcia-Castillo, C. Garcia-Stewart, S. Pegrum, S. Colbourne, P. Turner, S. D. Crossley, T. Litt, S. Murray, K. B. Ozanyan, and H. McCann, "High-speed chemical species tomography in a multi-cylinder automotive engine," *Chem. Eng. J.* **158**, 2–10 (2010).
- [16] S. A. Tsekenis, D. Wilson, M. Lengden, J. Hyvönen, J. Leinonen, A. Shah, Ö. Andersson, and H. McCann, "Towards in-cylinder chemical species tomography on large-bore IC engines with pre-chamber," *Flow Meas. Instrum.* **53**, 116–125 (2017).

- [17] J. Emmert, H. Schneider, C. Meißner, E. Sidiropoulos, J. I. Hölzer, T. Seeger, B. Böhm, A. Dreizler, and S. Wagner, "Characterization of temperature distributions in a swirled oxy-fuel coal combustor using tomographic absorption spectroscopy with fluctuation modelling," *Appl. Energy Combust. Sci.* **6**, 100025 (2021).
- [18] C. Liu, Z. Cao, Y. Lin, L. Xu, and H. McCann, "Online cross-sectional monitoring of a swirling flame using TDLAS tomography," *IEEE Trans. Instrum. Meas.* **67**, 1338–1348 (2018).
- [19] A. Upadhyay, M. Lengden, G. Enemali, G. Stewart, W. Johnstone, D. Wilson, G. Humphries, T. Benoy, J. Black, A. Chighine, E. Fisher, R. Zhang, C. Liu, N. Polydorides, A. Tsekenis, P. Wright, J. Kliment, J. Nilsson, Y. Feng, V. Archilla, J. Rodríguez-Carmona, J. Sánchez-Valdepeñas, M. Beltran, V. Polo, I. Armstrong, I. Mauchline, D. Walsh, M. Johnson, J. Bauldreay, and H. McCann, "Tomographic imaging of carbon dioxide in the exhaust plume of large commercial aero-engines," *Appl. Opt.* **61**, 8540–8552 (2022).
- [20] R. Zhang, J. Si, G. Enemali, Y. Bao, and C. Liu, "Spatially driven chemical species tomography with size-adaptive hybrid meshing scheme," *IEEE Sens. J.* **22**, 12728–12737 (2022).
- [21] W. Zhao, L. Xu, A. Huang, X. Gao, X. Luo, H. Zhang, H. Chang, and Z. Cao, "A WMS based TDLAS tomographic system for distribution retrievals of both gas concentration and temperature in dynamic flames," *IEEE Sens. J.* **20**, 4179–4188 (2019).
- [22] D. Liu, J. Wang, Q. Shan, D. Smyl, J. Deng, and J. Du, "DeepEIT: Deep Image Prior Enabled Electrical Impedance Tomography," *IEEE Trans. Pattern Anal. Mach. Intell.* **45**, 9627–9638 (2023).
- [23] K. J. Daun, S. J. Grauer, and P. J. Hadwin, "Chemical species tomography of turbulent flows: Discrete ill-posed and rank deficient problems and the use of prior information," *J. Quant. Spectrosc. Radiat. Transfer* **172**, 58–74 (2016).
- [24] R. Gordon, R. Bender, and G. T. Herman, "Algebraic reconstruction techniques (ART) for three-dimensional electron microscopy and X-ray photography," *J. Theor. Biol.* **29**, 471–481 (1970).
- [25] D. Verhoeven, "Limited-data computed tomography algorithms for the physical sciences," *Appl. Opt.* **32**, 3736–3754 (1993).
- [26] T. Elfving, P. C. Hansen, and T. Nikazad, "Semi-convergence properties of Kaczmarz's method," *Inverse Probl.* **30**, 055007 (2014).
- [27] J. Kaipio and E. Somersalo, *Statistical and Computational Inverse Problems*, vol. 160 (Springer Science & Business Media, 2006).
- [28] P. C. Hansen, *Rank-Deficient and Discrete Ill-posed Problems: Numerical Aspects of Linear Inversion* (SIAM, 1998).
- [29] H. McCann, P. Wright, K. Daun, S. J. Grauer, C. Liu, and S. Wagner, "Chemical species tomography," in "Industrial Tomography," (Elsevier, 2022), pp. 155–205.
- [30] K. J. Daun, "Infrared species limited data tomography through Tikhonov reconstruction," *J. Quant. Spectrosc. Radiat. Transfer* **111**, 105–115 (2010).
- [31] A. Guha and I. Schoegl, "Tomographic laser absorption spectroscopy using Tikhonov regularization," *Appl. Opt.* **53**, 8095–8103 (2014).
- [32] J. Dai, T. Yu, L. Xu, and W. Cai, "On the regularization for nonlinear tomographic absorption spectroscopy," *J. Quant. Spectrosc. Radiat. Transfer* **206**, 233–241 (2018).
- [33] Z.-T. Niu, H. Qi, Z.-Y. Zhu, K.-F. Li, Y.-T. Ren, and M.-J. He, "A novel parametric level set method coupled with Tikhonov regularization for tomographic laser absorption reconstruction," *Appl. Therm. Eng.* **201**, 117819 (2022).

- [34] Z.-T. Niu, H. Qi, S. Zheng, Y.-T. Ren, M.-J. He, F. Wang, and W.-J. Sun, "Nonlinear deflection tomography of inhomogeneous flame temperature and concentration based on topology evolution with prior smoothing," *Combust. Flame* **263**, 113398 (2024).
- [35] C. Wei, K. K. Schwarm, D. I. Pineda, and R. M. Spearrin, "Volumetric laser absorption imaging of temperature, CO and CO<sub>2</sub> in laminar flames using 3D masked Tikhonov regularization," *Combust. Flame* **224**, 239–247 (2021).
- [36] L. Ma and W. Cai, "Numerical investigation of hyperspectral tomography for simultaneous temperature and concentration imaging," *Appl. Opt.* **47**, 3751–3759 (2008).
- [37] L. Ma, X. Li, S. T. Sanders, A. W. Caswell, S. Roy, D. H. Plemmons, and J. R. Gord, "50-kHz-rate 2D imaging of temperature and H<sub>2</sub>O concentration at the exhaust plane of a J85 engine using hyperspectral tomography," *Opt. Express* **21**, 1152–1162 (2013).
- [38] W. Cai and C. F. Kaminski, "Multiplexed absorption tomography with calibration-free wavelength modulation spectroscopy," *Appl. Phys. Lett.* **104** (2014).
- [39] J.-W. Shi, H. Qi, J.-Y. Zhang, Y.-T. Ren, L.-M. Ruan, and Y. Zhang, "Simultaneous measurement of flame temperature and species concentration distribution from nonlinear tomographic absorption spectroscopy," *J. Quant. Spectrosc. Radiat. Transfer* **241**, 106693 (2020).
- [40] C. Wei, K. K. Schwarm, D. I. Pineda, and R. M. Spearrin, "Deep neural network inversion for 3D laser absorption imaging of methane in reacting flows," *Opt. Lett.* **45**, 2447–2450 (2020).
- [41] C. Wei, K. K. Schwarm, D. I. Pineda, and R. Mitchell Spearrin, "Physics-trained neural network for sparse-view volumetric laser absorption imaging of species and temperature in reacting flows," *Opt. Express* **29**, 22553–22566 (2021).
- [42] Y. Jiang, J. Si, R. Zhang, G. Enemali, B. Zhou, H. McCann, and C. Liu, "CSTNet: A Dual-Branch Convolutional Neural Network for Imaging of Reactive Flows Using Chemical Species Tomography," *IEEE Trans. Neural Networks Learn. Syst.* **34**, 9248–9258 (2023).
- [43] T. Yu, W. Cai, and Y. Liu, "Rapid tomographic reconstruction based on machine learning for time-resolved combustion diagnostics," *Rev. Sci. Instrum.* **89** (2018).
- [44] Z. Wang, N. Zhu, W. Wang, and X. Chao, "Y-Net: a dual-branch deep learning network for nonlinear absorption tomography with wavelength modulation spectroscopy," *Opt. Express* **30**, 2156–2172 (2022).
- [45] J. Si, G. Fu, Y. Cheng, R. Zhang, G. Enemali, and C. Liu, "A Quality-Hierarchical Temperature Imaging Network for TDLAS Tomography," *IEEE Trans. Instrum. Meas.* **71**, 1–10 (2022).
- [46] J. Si, G. Fu, X. Liu, Y. Cheng, R. Zhang, J. Xia, Y. Fu, G. Enemali, and C. Liu, "A Spatially Progressive Neural Network for Locally/Globally Prioritized TDLAS Tomography," *IEEE Trans. Ind. Inf.* **19**, 10544–10554 (2023).
- [47] S. Wang, X. Yu, and P. Perdikaris, "When and why PINNs fail to train: A neural tangent kernel perspective," *J. Comput. Phys.* **449**, 110768 (2022).
- [48] Y. Sun, J. Liu, M. Xie, B. Wohlberg, and U. S. Kamilov, "CoIL: Coordinate-based internal learning for tomographic imaging," *IEEE Trans. Comput. Imaging* **7**, 1400–1412 (2021).
- [49] K. Zhang, R. Guo, M. Li, F. Yang, S. Xu, and A. Abubakar, "Supervised Descent Learning for Thoracic Electrical Impedance Tomography," *IEEE Trans. Biomed. Eng.* **68**, 1360–1369 (2021).
- [50] G. Zang, R. Idoughi, R. Li, P. Wonka, and W. Heidrich, "IntraTomo: self-supervised learning-based tomography via sinogram synthesis and prediction," in "Proc. IEEE/CVF Int. Conf. Comput. Vision," (2021), pp. 1960–1970.

- [51] D. Rückert, Y. Wang, R. Li, R. Idoughi, and W. Heidrich, “Neat: Neural adaptive tomography,” *ACM Trans. Graphics* **41**, 1–13 (2022).
- [52] F. Zhang, W. Zhang, Q. Lei, X. Li, Y. Li, and M. Xu, “Voxel-free neural volume reconstruction technique for volumetric flame reconstructions,” *Aerosp. Sci. Technol.* **133**, 108107 (2023).
- [53] D. Kelly and B. Thurow, “Investigation of a neural implicit representation tomography method for flow diagnostics,” *Meas. Sci. Technol.* p. 118996 (2024).
- [54] J. P. Molnar, L. Venkatakrishnan, B. E. Schmidt, T. A. Sipkens, and S. J. Grauer, “Estimating density, velocity, and pressure fields in supersonic flows using physics-informed BOS,” *Exp. Fluids* **64**, 14 (2023).
- [55] J. P. Molnar, E. J. LaLonde, C. S. Combs, O. Léon, D. Donjat, and S. J. Grauer, “Forward and inverse modeling of depth-of-field effects in background-oriented schlieren,” *AIAA J.* pp. 1–14 (2024).
- [56] H. Li, T. Ren, and C. Zhao, “A physics-informed neural network for non-linear laser absorption tomography,” *J. Quant. Spectrosc. Radiat. Transfer* **24**, 109229 (2024).
- [57] R. R. Gamache, B. Vispoel, M. Rey, A. Nikitin, V. Tyuterev, O. Egorov, I. E. Gordon, and V. Boudon, “Total internal partition sums for the HITRAN2020 database,” *J. Quant. Spectrosc. Radiat. Transfer* **271**, 107713 (2021).
- [58] I. E. Gordon, L. S. Rothman, R. J. Hargreaves, R. Hashemi, E. V. Karlovets, F. M. Skinner, E. K. Conway, C. Hill, R. V. Kochanov, Y. Tan, P. Wcisło, A. A. Finenko, K. Nelson, P. F. Bernath, M. Birk, V. Boudon, A. Campargue, K. V. Chance, A. Coustenis, B. J. Drouin, J.-M. Flaud, R. R. Gamache, J. T. Hodges, D. Jacquemart, E. J. Mlawer, A. V. Nikitin, V. I. Perevalov, M. Rotger, J. Tennyson, G. C. Toon, H. Tran, V. G. Tyuterev, E. M. Adkins, A. Baker, A. Barbe, E. Canè, A. G. Császár, A. Dudaryonok, O. Egorov, A. J. Fleisher, H. Fleurbaey, A. Foltynowicz, T. Furtenbacher, J. J. Harrison, F. Kwabia-Tchana, N. N. Horneman, X. Huang, T. Karman, J. Karns, S. Kassi, I. Kleiner, V. Kofman, V. Kwabia-Tchana, N. N. Lavrentieva, T. J. Lee, D. A. Long, A. A. Lukashchinskaya, O. M. Lyulin, V. Makhnev, Yu. W. Matt, S. T. Massie, M. Melosso, S. N. Mikhailenko, D. Mondelain, H. S. P. Müller, O. V. Naumenko, A. Perrin, O. L. Polyansky, E. Raddaoui, P. L. Raston, Z. D. Reed, M. Rey, C. Richard, R. Tóbiás, I. Sadiek, D. W. Schwenke, E. Starikova, K. Sung, F. Tamassia, S. A. Tashkun, J. Vander Auwera, I. A. Vasilenko, A. A. Vignani, G. L. Villanueva, B. Vispoel, G. Wagner, A. Yachmenev, and S. N. Yurchenko, “The HITRAN2020 molecular spectroscopic database,” *J. Quant. Spectrosc. Radiat. Transfer* **277**, 107949 (2022).
- [59] L. S. Rothman, I. E. Gordon, R. J. Barber, H. Dothe, R. R. Gamache, A. Goldman, V. I. Perevalov, S. A. Tashkun, and J. Tennyson, “HITEMP, the high-temperature molecular spectroscopic database,” *J. Quant. Spectrosc. Radiat. Transfer* **111**, 2139–2150 (2010).
- [60] V. Morozov, “On the solution of functional equations by the method of regularization,” *Dokl. Akad. Nauk SSSR* **167**, 510 (1966).
- [61] E. O. Åkesson and K. J. Daun, “Parameter selection methods for axisymmetric flame tomography through Tikhonov regularization,” *Appl. Opt.* **47**, 407–416 (2008).
- [62] G. H. Golub, M. Heath, and G. Wahba, “Generalized cross-validation as a method for choosing a good ridge parameter,” *Technometrics* **21**, 215–223 (1979).
- [63] P. C. Hansen, “Analysis of discrete ill-posed problems by means of the L-curve,” *SIAM Rev.* **34**, 561–580 (1992).
- [64] S. Wang, Y. Teng, and P. Perdikaris, “Understanding and mitigating gradient flow pathologies in physics-informed neural networks,” *SIAM J. Sci. Comput.* **43**, A3055–A3081 (2021).
- [65] S. Wang, S. Sankaran, H. Wang, and P. Perdikaris, “An expert’s guide to training physics-informed neural networks,” *arXiv preprint arXiv:2308.08468* (2023).
- [66] S. Wang, X. Yu, and P. Perdikaris, “When and why PINNs fail to train: A neural tangent kernel perspective,” *J. Comput. Phys.* **449**, 110768 (2022).

- [67] T. Poinso, *Theoretical and Numerical Combustion* (RT Edwards, 2005).
- [68] M. Zhou, R. Zhang, Y. Chen, Y. Fu, J. Xia, A. Upadhyay, and C. Liu, "Large-Scale Data Processing Platform for Laser Absorption Tomography," *Meas. Sci. Technol.* (2024).
- [69] Y. Bao, R. Zhang, G. Enemali, Z. Cao, B. Zhou, H. McCann, and C. Liu, "Relative entropy regularized TDLAS tomography for robust temperature imaging," *IEEE Trans. Instrum. Meas.* **70**, 1–9 (2020).
- [70] M. V. Svechnikov, N. I. Chkhalo, M. N. Toropov, and N. N. Salashchenko, "Resolving capacity of the circular Zernike polynomials," *Opt. Express* **23**, 14677–14694 (2015).
- [71] K. Niu and C. Tian, "Zernike polynomials and their applications," *J. Opt.* **24**, 123001 (2022).
- [72] J. Xia, G. Enemali, R. Zhang, Y. Fu, H. McCann, B. Zhou, and C. Liu, "FPGA-Accelerated distributed sensing system for real-time industrial laser absorption spectroscopy tomography at kilo-hertz," *IEEE Trans. Ind. Inf.* (2023).
- [73] G. Enemali, R. Zhang, H. McCann, and C. Liu, "Cost-effective quasi-parallel sensing instrumentation for industrial chemical species tomography," *IEEE Trans. Ind. Electron.* **69**, 2107–2116 (2021).
- [74] C. S. Goldenstein, C. L. Strand, I. A. Schultz, K. Sun, J. B. Jeffries, and R. K. Hanson, "Fitting of calibration-free scanned-wavelength-modulation spectroscopy spectra for determination of gas properties and absorption lineshapes," *Appl. Opt.* **53**, 356–367 (2014).
- [75] C. S. Goldenstein, I. A. Schultz, J. B. Jeffries, and R. K. Hanson, "Two-color absorption spectroscopy strategy for measuring the column density and path average temperature of the absorbing species in nonuniform gases," *Appl. Opt.* **52**, 7950–7962 (2013).
- [76] A. Towne, O. T. Schmidt, and T. Colonius, "Spectral proper orthogonal decomposition and its relationship to dynamic mode decomposition and resolvent analysis," *J. Fluid Mech.* **847**, 821–867 (2018).
- [77] H. Sato, K. Amagai, and M. Arai, "Diffusion flames and their flickering motions related with Froude numbers under various gravity levels," *Combust. Flame* **123**, 107–118 (2000).
- [78] W. H. Press, *Numerical Recipes: The Art of Scientific Computing* (Cambridge University Press, 2007).
- [79] G. Jin, J. C. Wong, A. Gupta, S. Li, and Y.-S. Ong, "Fourier warm start for physics-informed neural networks," *Eng. Appl. Artif. Intell.* **132**, 107887 (2024).